Title

The Effect of Ethanol Consumption on Composition and Morphology of Femur Cortical Bone in Wild-Type and ALDH2*2-Homozygous Mice

Permalink

https://escholarship.org/uc/item/85f5h3wz

Journal

Calcified Tissue International, 108(2)

ISSN

0171-967X

Authors

Malkovskiy, Andrey V
Van Wassenhove, Lauren D
Goltsev, Yury
et al.

Publication Date

2021-02-01

DOI

10.1007/s00223-020-00769-1

Peer reviewed

The effect of ethanol consumption on composition and morphology of femur cortical bone in wild-type and ALDH2*2-homozygous mice

Andrey V. Malkovskiy[1,2,*], **Lauren D. Van Wassenhove**[2], **Yury Goltsev**[3], **Kwame Osei-Sarfo**[4], **Che-Hong Chen**[2], **Bradley Efron**[5], **Lorraine J. Gudas**[4], **Daria Mochly-Rosen**[2], **Jayakumar Rajadas**[1,*]

[1]Biomaterials and Advanced Drug Delivery Laboratory, Stanford Medical School, Stanford, CA 94305

[2]Department of Chemical and Systems Biology, Stanford Medical School, Stanford, CA 94305

[3]Department of Microbiology and Immunology, Baxter Laboratory in Stem Cell Biology, Stanford Medical School, Stanford, CA 94305

[4]Department of Pharmacology, Weill Cornell Medical College, New York, NY 10065

[5]Department of Biomedical Data Science, Stanford Medical School, Stanford, CA, 94305.

Abstract

ALDH2 inactivating mutation (ALDH2*2) is the most abundant mutation leading to bone morphological aberration. Osteoporosis has long been associated with changes in bone biomaterial in elderly populations. Such changes can be exacerbated with elevated ethanol consumption and in subjects with impaired ethanol metabolism, such as carriers of aldehyde dehydrogenase 2 (ALDH2)-deficient gene, ALDH2*2. So far, little is known about bone compositional changes besides a decrease in mineralization. Raman spectroscopic imaging has been utilized to study the changes in overall composition of C57BL/6 female femur bone sections, as well as in compound spatial distribution. Raman maps of bone sections were analyzed using multilinear regression with these four isolated components, resulting in maps of their relative distribution. A 15-week treatment of both wild-type (WT) and ALDH2*2/*2 mice with 20% ethanol in the drinking water resulted in a significantly lower mineral content ($p < 0.05$) in the bones. There was no significant change in mineral and collagen content due to the mutation alone ($p > 0.4$). Highly localized islets of elongated adipose tissue were observed on most maps. Elevated fat content was found in ALDH2*2 knock-in mice consuming ethanol ($p < 0.0001$) and this effect appeared cumulative. This work conclusively demonstrates that that osteocytes in femurs of older female mice accumulate fat, as has been previously theorized, and that fat accumulation is likely modulated by levels of acetaldehyde, the ethanol metabolite.

*corresponding authors: malkovskiy@gmail.com; jayraja@stanford.edu.

Mini Abstract

Little is known about bone compositional changes in human subjects with ALDH2 gene deficiency besides decreases in mineralization, particularly in case of chronic alcohol consumption. Our Raman and fluorescence imaging of femur sections of ADLH2*2 knock-in and alcohol-consuming C57BL/6 9-months old female mice also show accumulation of fat in osteocytes.

Keywords

Introduction

Osteoporosis and osteopenia are common problems associated with aging; one in three women and one in five men over the age of 50 experience osteoporosis-induced fractures in their lifetime, greatly adding to their morbidity and mortality [1,2]. Diminished bone quality, decreased bone density, and increased adipose tissue [3] in bone marrow of humans and rats are greater in alcoholic subjects [3–6]. In humans, alcohol is first metabolized to acetaldehyde by alcohol dehydrogenase (ADH) and acetaldehyde is further detoxified to acetate by aldehyde dehydrogenase 2 (ALDH2) [7]. Approximately 560 million East Asians cannot process acetaldehyde properly due to the lack of a functional ALDH2 enzyme [8], which is caused by a common dominant inactivating point mutation in the ALDH2 gene denoted as the ALDH2*2 mutation [9]. ALDH2*2 is a dominant negative mutation [10–12]. ALDH2 is a tetramer. A single monomer is not active, only a pair of dimers can form a catalytic and NAD co-factor binding site. In addition, ALDH2*2 is more labile, affecting the half-life of the WT monomers in the heterotetramer. Carriers of the inactive ALDH2*2 gene are three times more likely to develop osteoporosis [13] and higher risk of hip fracture [14]. With the administration of ethanol for 4 weeks, differentiation and mineralization of osteoblasts was severely suppressed resulting in reduced trabecular bone formation and bone volume in these ALDH2–/– knock-in mice [15]. The lack of consistency in the observed results for the different mouse mutant and ethanol treatment models suggests that there are compositional changes beyond simple changes in overall mineralization.

Bone mineral density (BMD) via X-ray absorptiometry (DXA) scans [16] is used in the clinic to identify patients at risk of osteopenia or osteoporosis. This method, although valuable in the clinic, does not provide the robust data necessary to characterize the bone at the molecular level, which is necessary to assess the efficacy of potential therapies since the changes to BMD are small and delayed [15]. The main reason behind studying cortical bone shafts of mouse femur is that these tissues bear most of the load. While an earlier study [15] reported decreases in trabecular bone mineralized nodule formation for ALDH2 knock-in mice consuming ethanol, the effect in the rodent model of ALDH2*2 knock-in of the human mutation has not been studied.

BMD and other aspects of bone quality have been measured in rodents, *ex vivo*. These studies have involved measuring gross morphological changes as well as physical properties,

such as bone size, thickness, and brittleness [17, 18]. Bone marrow adipose tissue has been quantified by dual-energy computerized tomography (DECT) [19] and magnetic resonance imaging [20]. More recent work applying Fourier transform infrared (FTIR) microscopy [21–26] to assess bone quality and map mineral distribution [27–29].

Raman spectroscopy, like infrared (IR) imaging, detects vibrational and rotational motions of atoms and thus is very effective in detecting chemical composition of materials and tissues. Raman spectroscopy has increased spectral resolution and lack of signal interference due to water signal that plagues FTIR [22, 30]. Importantly, Raman mineral density measurements were shown to align with DXA data for the same specimens [31]. Although Raman has been previously used to analyze bone samples for single-point measurements [32–35] and to map areas based on amide and mineral peaks [36–38] this study represents the first complete Raman spectral imaging of rodent bone utilizing the entire fingerprint spectral range up to 3200 cm^{-1}. Multi-Linear Regression (MLR) fitting over the entire Raman spectrum, utilizing all chemical signature bands, is required to be able to accurately distinguish between fat and collagen signals. MLR technique has been applied very recently with great success to distinguish between different redox states of mitochondria [39], as well as for more clear imaging of individual cell subcomponents [40].

In this paper, we propose a model that mouse cortical bone consists of four primary components that comprise most of the content: mineral, collagen, proteoglycans and fat. Such components could then be mapped by Raman across a bone section and their abundance measured, providing useful insights into compositional differences between cortical bones of old WT mice, old mice after extensive ethanol treatment, old mice with ALDH2*2 transgenic knock-in mutation developed earlier in the lab and old mice with both a mutation and ethanol treatment. Mineralization data obtained in this way should be consistent with CT results.

It should be noted here that the assumption of four-component composition of cortical bone is, of course, a simplification of the complex bone structure. There are several limitations of the model. The bone has additional components such as osteocalcin. However, osteocalcin must have a strong amide band, which is clearly not a characteristic of our empirically determined "average bound proteoglycan" compound. Thus, due to relatively low abundance in the scanned areas, the osteocalcin signal is buried below the noise level for low acquisition times. More complex Raman techniques, such as resonance Raman, or higher laser powers are required for this. There can also be several types of proteoglycans, collagens and fats present. The differences in their spectra are quite small and, similarly, were found to be below the detection limit of our set-up. Finally, the individual components can exhibit shape and position changes for their primary peaks, depending on short and medium-order interactions with other components. However, as we have witnessed in our studies [41, 42], even extremely strong interactions, despite significant changes to a few individual peaks, do not change the shape of the whole spectrum dramatically, highlighting yet another advantage of using MLR analysis instead of traditional peak integrations and deconvolutions.

The primary aim of the paper was to test whether Raman mapping could be a viable and inexpensive alternative to different CT techniques in detecting changes in mouse femur diaphysis mineralization. In addition, by using the four-component Raman model, as well as supporting techniques, we wanted to test our hypothesis that the reduced ability to detoxify aldehydes due to ALDH2*2 inactivating mutation affects bone composition and that the increased aldehydic load through chronic exposure to ethanol will further exacerbate altered bone composition.

Materials and Methods

Knock-in mouse model

The ALDH2*2 knock-in mice have been generated from C57BL/6 mice by using homologous recombination to replace the mouse ALDH2 allele with the mutant E487K ALDH2 mutant allele according to the procedures described by Zambelli et al. [43]. Both wild-type controls and ALDH2 homozygous (ALDH2*2/*2) were fed standard rodent chow, ad libitum, provided by the Research Animal Resource Center (RARC) at Weill Cornell Medical College. For details on ethanol treatment and its effects on mice, refer to Osei-Sarfo et al. [44, 45]. As this was a chronic study, with samples split between multiple techniques, we have added 6 samples to the 1st group (WT) *post hoc*, purchased from Jackson Laboratories, to improve significance of the results, as these were the only samples that could be obtained commercially.

Mouse treatment details

Mice were treated according to the Administrative Panel on Laboratory Animal Care (APLAC) guidelines, at Weill Cornell Medical College of Cornell University. All applicable institutional and/or national guidelines for the care and use of animals were followed. Wild type (ALDH2*1/*1) and homozygous (ALDH2*2/*2) female C57BL/6 mice at 21 weeks of age were given either water or 20% ethanol for 15 weeks. The homozygosity of the mutant mice was confirmed by PCR. The water with 20% ethanol was replaced weekly as described [44]. Mice were euthanized by cervical dislocation, skin removed, and legs were shipped in PBS under refrigeration/on ice to Stanford University, where the bones were cleaned from soft tissue.

Mouse bone preparation

The same set of bone samples from 9-month old mice from 4 treatment groups was used for Raman, microCT and Fluorescence imaging. Flat longitudinal cross-sections were prepared by consecutive slicing of cryosections in OCT compound (ThermoFischer Scientific, Waltham, MS, US) in Leica CM1950 cryostat until half of the bone along the major leg direction was removed (Fig. 1). We used C.L.Sturkey, Inc.® high profile heavy duty disposable knives for sectioning. A new location on the blade was used for every sample by sliding the knife along the holder, until most of it was used. Then, a new knife was taken. This resulted in most sections being clean and smooth. The few non-smooth sections were not used for further experiments and were discarded. For Raman, the resulting sample was placed in a mold of air-hardening clay in such a way that the cross-section surface was perpendicular to the microscope objective. After hardening in air for a day, the mold

provided a holder for the bone sample that maintained it perpendicular to the objective for more than a week. We have added 6 samples to the 1st group (WT mice given water) *post hoc*, purchased from Jackson Laboratories, to improve significance of the results, as these were the only samples that could be obtained commercially. For fluorescence experiments, the samples were embedded in OCT and sliced into 8-μm thin sections in a Leica CM3050 S cryostat with assistance of Kawamoto film [46]. For color staining, full-length bones were fixed in formalin for 24 hours and then stored in ethanol for 72 hours. Bones were then decalcified, paraffin embedded, sectioned and H&E stained if applicable by Histo-Tec Laboratory Inc. (Hayward California). For all experiments, we used the middle of mouse femur diaphysis, unless indicated otherwise.

Histology and optical imaging

Bone sections were stained using the BIC staining protocol described in [47]. Color images of stained sections of full-length femurs were acquired using an All-in-One Fluorescence Microscope BZ-X700 (Keyence).

Raman spectroscopy imaging

Mouse bone sections were prepared directly by cryosectioning bone samples embedded in OCT compound without any additional treatment or decalcification, to preserve the original composition, perpendicular to the microscope imaging plane. Raman experiments were performed with NTEGRA™ Spectra Raman spectrophotometer instrument, equipped with a peltier plate-cooled CCD camera in backscattering geometry. The illumination source was a 473 nm Cobolt Blues™ continuous wave diode-pumped solid-state laser brought to the sample by a Mitutoyo long working distance objective (100X, 0.7 NA). Raman pinhole was set at 120 microns, so the resulting focal spot was expected to be around 0.8 microns in diameter. Laser power at sample was ~2 mW, as measured by Coherent LaserCheck™. Nine samples were used for WT group and three for other groups, and average of 3 scan areas per bone was provided. Images were 80×80 microns with 1 micron step in each axis, 10 s Raman acquisition per pixel. Intensity maps were plotted with the help of LabView CW3DGraph ActiveX visualization packages.

Raman of pure materials

Pure dry hyaluronic acid, chondroitin sulphate and heparin were purchased from Aldrich (heparin) and Sigma-Aldrich, US. Raman measurements were taken directly from crystalline solids.

Unbiased separation of Raman spectra of bone into four principle components

Individual Raman spectra were analyzed, and curves were identified with the strongest contribution of a specific features, i.e. the C-H broad peaks at 2850–3000 cm^{-1} or the sharp PO_4^{3-} peak at 962 cm^{-1}. Our model assumes that all Raman spectra represent a superposition of four primary components: collagen tissue, mineral deposits, fat/adipose tissue and bound proteoglycans. Due to our experimental conditions, different types of collagens, proteoglycans and fats could not be reliably distinguished. Each individual spectrum with prominent features of one type was corrected for other components, thus

effectively separating the principal chemical compounds. Spectrum for each of the components with the most profound Raman bands in a specific region were isolated by Gaussian elimination, using experimental spectra with the highest signal. The resulting spectra can be seen in Fig. 1, right panel. The results were confirmed by repeating this analysis for three spots, on average. These isolated components were used to fit every spectrum of the Raman maps of bone sections, and to determine the contribution of each component in the composition of the bone tissue, using MLR fit, with an algorithm that we have developed in LabView. In addition to the sum of the four components, a simple second order polynomial line was sufficient to compensate for the fluorescent background, which resulted in highly satisfactory performance even for spots with elevated fluorescence. The principle of MLR fitting is described below and illustrated in Fig. 1. For more information, the reader can refer to the following reference whose authors have developed a similar MLR spectral fitting method independently [39].

Multilinear Regression (MLR) fitting

A successful fit of four pure components to Raman data for every pixel on the 81 by 81 microns image was a result of minimizing chi-square residual for a set of 1020 equations (number of horizontal pixels on the Raman spectrometer CCD matrix) by Levenberg-Marquardt algorithm for non-linear curves, such that:

$$f(x) = a_0 + a_1 \, y_{collagen}(x) + a_2 \, y_{mineral}(x) + a_3 \, y_{fat}(x) + a_4 \, y_{proteoglycan}(x) + a_5 \, x^2 + a^6 x$$

for x from 1 to 1024, where $y_{collagen}$, $y_{mineral}$, y_{fat} and $y_{proteoglycan}$ are intensities of pure component Raman curves at position of x. The results of the fit a_1, a_2, a_3 and a_4 are contributions of the pure components in any spot of the map. As mentioned in the text, a second order polynomial was added to correct for elevated fluorescent background.

Statistics

Non-parametric permutation (coded in LabView) and T-tests with Welch's adjustment for differing variances have been performed on the Raman mineral, proteoglycan and fat data. Permutation tests tend to be exact significance tests for calculations of pooled average values and more robust than T-tests. For fluorescence data analysis, due to a very large number of points, only T-tests with Welch's adjustment were used. Significance levels are marked as follows: * $p < 0.05$, ** $p < 0.01$, **** $p < 0.0001$. For very low p values, they are written directly in the figures. Error bars correspond to standard deviation of data from mean values.

Micro-computed tomography

The entire length of cortical bones used for the Raman experiments were imaged by microCT using Bruker SkyScan1276™ instrument. Due to a lack of abrupt shift from cortical to trabecular bone in bone density signal, we imaged only the areas completely within the cortical region. The samples for each different group were imaged simultaneously with voxel size of 6 microns, attenuation filters of 0.25 and 1 mm Al. Each scan was acquired using the settings of 55 kV, 367 ms exposure for 0.25 mm Al and 85 kV, 345 ms exposure for 1 mm Al, 200 μA; 0.4° step size, no detector binning and frame averaging.

After acquisition of images, 2D reconstruction to a 6 μm isotopic voxel size was performed using NRecon software and the InstaRecon processing interface with 0.5 mm fine-tuning accuracy. Reconstructed data was analyzed in CTAn software. To match the conditions of the Raman experiment, each experimental data-point was taken as the BMD value for a 1-mm long section of the cortical bone, resulting in several sections per bone sample. The data-points were pooled for each sample. The final BMD values were obtained after appropriate calibration with primary instrument standards.

Fluorescence imaging

Nile Red fluorescent stain, which becomes fluorescent in non-polar environment (Aldrich) was dissolved in acetone to prepare the stock solution (8mg/ml) and then to a final concentration of 1 μg/mL in 5% BSA in PBS to facilitate cell permeation [48]. Samples were incubated in the dye solution for 10 min, followed by several washes with 5% BSA in PBS to remove excess dye. Images were collected using a Keyence BZ-X710 fluorescent microscope with 360/40 excitation and 460/50 nm emission filters and equipped with Nikon PlanFluor 40x NA 1.3 oil immersion lens. We have quantified osteocytic fat by measuring relative fat for every osteocyte from multiple images (6/6/9/10 images per group, respectively). This was done by placing a section across every osteocyte in ImageJ and calculating the relative local fluorescence intensity as *(Fat(osteocyte)-Fat(baseline))/ Fat(baselne)*. This way, overexposure and bleaching of fluorescence were properly accounted for.

Results

Assignment of Raman spectra of bone components and validation with standards

The isolated spectra were obtained using an unbiased method. Confirmation of the validity of this unbiased method was made in the observation that the resulting full fat spectrum was almost identical to that of corn oil (Fig. S1) [49] or sunflower oil over the entire spectral range [50]. The intensity of the 850 cm^{-1} and 1266 cm^{-1} peaks suggest the fat in regions we determined to be osteocytes, based on comparison of optical images with those from literature [51], is almost purely oleic acid [52]. The spectrum is also similar to the spectra of visceral and subcutaneous adipose tissue [53], which themselves are almost indistinguishable from each other by Raman spectra. Similarly, the mineral spectrum contained all the characteristic phosphate and carbonate bands, as expected from literature [31]. The spectrum of collagen in tissue shows some variation, due to strong dependence of amide band intensities on fibril orientation [54], but not for our Raman maps, as the fibrils generally are co-aligned with the longitudinal direction of the femur shaft. The ratio of the 1440 cm^{-1} CH band to amide I band at ~1640 cm^{-1} is consistent with a ratio of ~2.3 carbon atoms per one nitrogen [55]. The spectrum of bound proteoglycans was obtained by subtracting a spectrum with laser polarization perpendicular to the collagen fibrils, i.e. perpendicular to the femur shaft, from the spectrum with polarization along the shaft, as proteoglycan signal, unlike collagen, should not depend on laser polarization, and was corrected for mineral and fat signal. For example, purified proteoglycan spectra from several areas (Fig. S1b) show variations in the intensities of 958 cm^{-1}, 1368 cm^{-1} and 1048 cm^{-1} peaks, which likely correspond to C-S and C-H bands of glycosaminoglycans (Fig. S1c) and

local phosphorylation, respectively. However, the most pronounced features, and, consequently, the ones contributing the most to Raman maps, such as the low intensity of the amide I band and the position of the 1440 cm^{-1} C-H band, were very similar for most spots. Thus, we utilize the words "bound proteoglycans" to account for a mixture of proteoglycans in relatively homogeneous areas we were imaging.

Histology and optical staining further validate MLR fit and components

Demineralized cross-sections on glass slides were prepared from bones embedded in paraffin and stained with H&E or Bone-Inflammation-Cartilage (BIC) stain [47]. The latter was sensitive to proteoglycans. The adjacent sections were studied by Raman mapping. MLR fitting was done assuming six components: collagen, mineral, bound proteoglycans, fat, glass and paraffin. Raman spectra for the two latter compounds were collected from bulk glass slide and paraffin sections respectively. The maps of several areas within cortical and trabecular bone are presented in Fig. 2 and Fig. S2. As expected, glass maps correlate well with holes in the section. There is still residual mineral signal present throughout the specimens, approximately 20 times weaker than for bones that were not de-mineralized, with higher mineral content correlating with regions stained blue in H&E stain, as a result of diminished relative collagen content. The hydrophobic nature of fats, correlates well with maps of unwashed paraffin, making detection non-informative. Proteoglycan BIC staining in all images correlates with Raman maps of trabecular bone (Fig. 2, Fig. S2b,c), validating our initial assignment of its Raman spectrum. Profound proteoglycan content is observed in the growth plate regions of trabecular bone in femurs of ALDH2*2 homozygotic mice that consumed 20% ethanol in their drinking water for 15 weeks (ALDH2*2+EtOH).

Raman imaging shows decreased mineralization in alcohol-consuming mice, no additional change for mutant mice

In Fig. 3, two maps of the four component distributions from Raman were plotted for each condition as an example. Total values of component content were calculated by summing the respective relative percentages in each pixel for the Raman images (Fig. 4). Samples prepared in this manner are very robust, as an ALDH2*2+EtOH section was imaged fresh and after 30 days in air at room temperature with no significant difference between images, except for minimal focus drift were observed in the maps of the components or their integrated content (Fig. S3).

Our study shows that there is a significant difference in the relative amount of mineral and bone materials between mice that chronically consume ethanol and those without ethanol exposure. This was observed both for WT ($p = 0.014$) and ALDH2*2 ($p = 0.05$) mice cohorts. No significant difference in mineralization was observed between WT and ALDH2*2 mice, regardless of ethanol treatment ($p = 0.545$ (no EtOH); 0.4 (w/ EtOH)). This correlates well the findings of Tsuchiya *et. al*, which found no difference for ultimate load and stiffness between WT and ALDH2 knock-in mice [17], whereas ethanol-treated rodents generally have much lower bone stiffness and elastic modulus [19].

ALDH2*2 mutation as well as alcohol exposure results in osteocyte fat accumulation

In addition to differences in mineralization of WT and ethanol-treated mice, there appeared to be a difference between fat content in bones, as determined by integrating fat content over the entirety of each image (Fig. 4b), although only the WT and ALDH2*2+EtOH groups showed statistical significance (p = 0.041) due to big data scatter. To confirm the finding of fat accumulation in osteocytes, we have performed fluorescent lipid staining with Nile Red dye [48] on the same samples, which were frozen in OCT and sliced into 8-μm thin sections in a microtome. Fat in osteocytes shows distinct elongated shapes (Fig. 5). The ALDH2*2 knock-in mutation results in ~1.5 times increase in osteocytic fat (p = $6.2*10^{-5}$), the alcohol treatment increases fat ~3-fold for both WT (p = $4.5*10^{-14}$) and ALDH2*2 mice (p = $5.1*10^{-27}$)(Fig. 4d). Consequently, their combination results in a cumulative effect of 4.5-fold increase. This is in general agreement with Raman results (Fig. 4c). Fluorescence results, however, show that WT+EtOH samples have accumulated more fat than ALDH2*2 samples without ethanol treatment. Since there is higher uncertainly in Raman results, we believe the results of fluorescence imaging are more reliable and conclusive.

Discussion

To confirm the lower mineral content of alcohol-consuming mice in Raman results, we have also performed micro computed tomography (microCT) experiments (Fig. 6). The BMD values, were lower for ethanol-consuming groups (1.428 ± 0.075 for WT+EtOH, 1.426 ± 0.023 for ALDH2*2+EtOH), than those without ethanol in their diet (1.457 ± 0.066 for WT, 1.447 ± 0.075 for ALDH2*2). The difference, however, was much smaller than for Raman results and, ultimately, was not statistically significant due to high data scatter and a small number of samples (p=0.2 for WT vs WT+EtOH, p=0.4 for ALDH2*2 vs ALDH2*2+EtOH). As with Raman, there appeared to be no difference between WT and knock-in mice. Different choices for the beam energy attenuation filters (0.25 mm Al, 1 mm Al) and density threshold in the CT analysis to include or exclude softer regions of the bone resulted in same or smaller difference between groups.

The lack of significant differences in mineralization, as observed in Raman and microCT experiments, between WT and ALDH2*2 mice, with same ethanol treatment or lack of it, correlates well the findings of Tsuchiya et. al, who found no difference for ultimate load and stiffness between WT and ALDH2 knock-in mice [17]. The ethanol treated groups had significantly lower mineral content in femur diaphysis. It was shown that ethanol-treated rodents generally have much lower bone stiffness and elastic modulus [19], decreased bone density and lower mineralization [56], as well as increased bone marrow adiposity [57]. Since the correlation of ratios of mineral to collagen Raman peaks to bone's Young's [58, 59] and compression [36] moduli have been established, this allows us to conclude that 15-week 20% ethanol treatment results in comparable decreases in bone strength for WT and ALDH2*2 mice alike.

Increased fat content in cortical bones, as observed from Raman and fluorescence imaging experiments, matches what we might expect from the ALDH2*2 phenotype of slow ethanol and acetaldehyde metabolism. Small islets of fat surrounded by areas of almost fat-free tissue are present in the images of all groups both in Raman and in fluorescence images,

although fluorescence appears to be worse at detecting fat in WT samples, due to background fluorescence signal from the surrounding tissue. These islets match osteocyte positions in optical images (Fig. S4), it has also been suggested recently that lipids accumulate in rat osteocytes [60]. The islets tend to be larger and have much higher fat content in ethanol-consuming and ALDH2*2 mice. This observation correlates with the findings of enlarged osteocytes for immobilized rats [51]. To the best of our knowledge and the accuracy of the experimental techniques, the data presented in the paper, for the first time, suggests that fat in cortical bone accumulates primarily in osteocytes and that this is exacerbated by ethanol consumption. Finally, our results show that bound proteoglycan distribution in cortical bone largely correlates with the position of osteocytes, while also occupying the area adjacent to it. This may be evidence of osteocyte "tethering" to the canaliculi walls, as first demonstrated by You et al. [61]. Our work suggests that proteoglycans may indeed be this tether, and further study will be needed to determine their exact identity.

Food consumption, liquid intake, mouse mass, and blood alcohol content was measured earlier [40] for the same wild-type C57BL/6 mice as used for this study (Fig. S5). Our results showed the same caloric and liquid intake in ethanol and water treated mice. Additionally, previous studies found that the Cook-Meadows model of chronic alcohol abuse had no significant change in mass of ethanol-treated (20%, final w:v concentration). C57BL/6 mice compared to mass of non-treated mice over a 12 week period [62]. Additionally, this study demonstrated the tolerance of multiple final concentrations of ethanol in seven murine strains. It was shown that 20% ethanol was the highest tolerance that C57BL/6 mice could handle without adverse effects. Multiple studies where 20% ethanol was administered by the Cook-Meadows model (single bottle, no choice method) have been reviewed in D'Souza et al. [63]. Similarly, our experiments on ALDH2*2/2 mice show that they could handle the 20% ethanol administration without a significant loss of weight (Fig. S5c). Thus, the mice did not experience any significant caloric restriction that would cause significant fat infiltration into bone, which suggests the changes in bone composition we observe come primarily from ethanol consumption.

The advantages of simultaneous Raman mapping and MLR analysis of collagen, mineral, bound proteoglycans and fat components in mouse leg longitudinal bone sections even for samples with elevated fluorescence are numerous. The current study required relatively simple sample preparation and instrumentation that is commonplace and less expensive than microCT. The spectra acquired from bone samples were analyzed by fully automated and unbiased baseline correction algorithms and were consistent for all samples measured irrespective of measurement conditions. Consequently, relative content of these components can be directly compared between samples, which is more accurate than comparing ratios of collagen amide-I and mineral phosphate bands that has been reported in literature to date. Higher spectral and spatial resolution than FTIR imaging allows visualizing morphologic features not able to be observed with FTIR, such as fat. Finally, a more in-depth analysis of component distribution is possible when additional isolated component spectra are introduced, (e.g. different types of matrix collagens, adipose tissues, mineral sub-components).

In summary, we have studied the effects of sustained ethanol consumption on femur diaphysis mineralization in WT and ALDH2*2 knock-in mice that were generated from C57BL/6 mice by using homologous recombination to replace the mouse ALDH2 allele with the mutant E487K ALDH2 mutant allele. Differences were observed in color staining and microCT experiments; fluorescence and Raman imaging showed significant differences in bone composition. Raman imaging and subsequent MLR analysis produced relative compound content images with qualitative results which were in agreement with those obtained with other techniques. Moreover, the compound maps visualized the general localization of fat and proteoglycans to osteocytes. Our results show that a 15-week consumption of 20% ethanol by both WT and ALDH2*2/*2 mice resulted in a significantly decreased mineral content and increased collagen content in bones. Fat content has also been found to be increased in ALDH2*2 mutant mice and a cumulative effect is observed in those consuming ethanol. Fat accumulation and relevant proteoglycan rearrangement can be the elusive factor making otherwise compositionally similar bone much more brittle. Carriers of the inactive ALDH2*2 gene have a three-fold increased adjusted odds for developing osteoporosis [13] and high risks of hip fracture [14]. This can have important immunological implications, as it was shown that there is a solid correlation between tumor necrosis factor (TNF-α), interleukin-6 (IL-6), and C-reactive protein and plasma levels of free fatty acids [64].

Supplementary Material

Refer to Web version on PubMed Central for supplementary material.

Acknowledgements

References

1. Katsoulis M, Benetou V, Karapetyan T, et al. (2017) Excess mortality after hip fracture in elderly persons from Europe and the USA: the CHANCES project. J Intern Med 281:300–310 [PubMed: 28093824]

2. Sözen T, Özı ık L, Ba aran NÇ (2017) An overview and management of osteoporosis. Eur J Rheumatol Inflamm 4:46–56

3. Maurel DB, Boisseau N, Benhamou CL, Jaffre C (2012) Alcohol and bone: review of dose effects and mechanisms. Osteoporos Int 23:1–16 [PubMed: 21927919]

4. Chakkalakal DA (2005) Alcohol-Induced Bone Loss and Deficient Bone Repair. Alcoholism: Clinical & Experimental Research 29:2077–2090

5. Mikosch P (2014) Alcohol and bone. Wien Med Wochenschr 164:15–24 [PubMed: 24477631]

6. Kim MJ, Shim MS, Kim MK, et al. (2003) Effect of Chronic Alcohol Ingestion on Bone Mineral Density in Males without Liver Cirrhosis. The Korean Journal of Internal Medicine 18:174–180 [PubMed: 14619387]

7. Zakhari S (2006) Overview: how is alcohol metabolized by the body? Alcohol Res 29:245

8. Brooks PJ, Enoch M-A, Goldman D, et al. (2009) The alcohol flushing response: an unrecognized risk factor for esophageal cancer from alcohol consumption. PLoS Med 6:e50 [PubMed: 19320537]

9. Yoshida A, Huang IY, Ikawa M (1984) Molecular abnormality of an inactive aldehyde dehydrogenase variant commonly found in Orientals. Proc Natl Acad Sci U S A 81:258–261 [PubMed: 6582480]

10. Steinmetz CG, Xie P, Weiner H, Hurley TD Structure of mitochondrial aldehyde dehydrogenase: the genetic component of ethanol aversion. (1997) Structure 5:701–711. [PubMed: 9195888]

11. Ni L, Zhou J, Hurley TD, Weiner H. Human liver mitochondrial aldehyde dehydrogenase: three-dimensional structure and the restoration of solubility and activity of chimeric forms. (1999) Protein Sci 8:2784–2790. [PubMed: 10631996]

12. Larson HN, Weiner H, Hurley TD. Disruption of the coenzyme binding site and dimer interface revealed in the crystal structure of mitochondrial aldehyde dehydrogenase "Asian" variant. (2005) J Biol Chem 280(34):30550–30556 [PubMed: 15983043]

13. Yamaguchi J, Hasegawa Y, Kawasaki M, et al. (2006) ALDH2 polymorphisms and bone mineral density in an elderly Japanese population. Osteoporos Int 17:908–913 [PubMed: 16520888]

14. Takeshima K, Nishiwaki Y, Suda Y, et al. (2017) A missense single nucleotide polymorphism in the ALDH2 gene, rs671, is associated with hip fracture. Scientific Reports 7

15. Shimizu Y, Sakai A, Menuki K, et al. (2011) Reduced bone formation in alcohol-induced osteopenia is associated with elevated p21 expression in bone marrow cells in aldehyde dehydrogenase 2-disrupted mice. Bone 48:1075–1086 [PubMed: 21256255]

16. Briot K (2013) DXA parameters: beyond bone mineral density. Joint Bone Spine 80:265–269 [PubMed: 23622733]

17. Tsuchiya T, Sakai A, Menuki K, et al. (2013) Disruption of aldehyde dehydrogenase 2 gene results in altered cortical bone structure and increased cortical bone mineral density in the femoral diaphysis of mice. Bone 53:358–368 [PubMed: 23313283]

18. Garcia JAD, Souza ALT, Cruz LHC, et al. (2015) Effects of ethanol consumption and alcohol detoxification on the biomechanics and morphology the bone in rat femurs. Braz J Biol 75:983–988 [PubMed: 26675916]

19. Bredella MA, Daley SM, Kalra MK, et al. (2015) Marrow Adipose Tissue Quantification of the Lumbar Spine by Using Dual-Energy CT and Single-Voxel (1)H MR Spectroscopy: A Feasibility Study. Radiology 277:230–235 [PubMed: 25988401]

20. Cordes C, Baum T, Dieckmeyer M, et al. (2016) MR-Based Assessment of Bone Marrow Fat in Osteoporosis, Diabetes, and Obesity. Front Endocrinol 7:74

21. Burghardt AJ, Wang Y, Elalieh H, et al. (2007) Evaluation of fetal bone structure and mineralization in IGF-I deficient mice using synchrotron radiation microtomography and Fourier transform infrared spectroscopy. Bone 40:160–168 [PubMed: 16905376]

22. Sivakumar S, Khatiwada CP, Sivasubramanian J (2014) Studies the alterations of biochemical and mineral contents in bone tissue of mus musculus due to aluminum toxicity and the protective action of desferrioxamine and deferiprone by FTIR, ICP-OES, SEM and XRD techniques. Spectrochimica Acta Part A: Molecular and Biomolecular Spectroscopy 126:59–67

23. Sen I, Bozkurt O, Aras E, et al. (2015) Lipid Profiles of Adipose and Muscle Tissues in Mouse Models of Juvenile Onset of Obesity without High Fat Diet Induction: A Fourier Transform Infrared (FT-IR) Spectroscopic Study. Applied Spectroscopy 69:679–688 [PubMed: 26054332]

24. Addison WN, Nelea V, Chicatun F, et al. (2015) Extracellular matrix mineralization in murine MC3T3-E1 osteoblast cultures: an ultrastructural, compositional and comparative analysis with mouse bone. Bone 71:244–256 [PubMed: 25460184]

25. Ross RD, Mashiatulla M, Robling AG, et al. (2016) Bone Matrix Composition Following PTH Treatment is Not Dependent on Sclerostin Status. Calcif Tissue Int 98:149–157 [PubMed: 26514840]

26. Vrahnas C, Pearson TA, Brunt AR, et al. (2016) Anabolic action of parathyroid hormone (PTH) does not compromise bone matrix mineral composition or maturation. Bone 93:146–154 [PubMed: 27686599]

27. Ling Y, Rios HF, Myers ER, et al. (2005) DMP1 depletion decreases bone mineralization in vivo: an FTIR imaging analysis. J Bone Miner Res 20:2169–2177 [PubMed: 16294270]

28. Verdelis K, Ling Y, Sreenath T, et al. (2008) DSPP effects on in vivo bone mineralization. Bone 43:983–990 [PubMed: 18789408]

29. Aido M, Kerschnitzki M, Hoerth R, et al. (2015) Effect of in vivo loading on bone composition varies with animal age. Exp Gerontol 63:48–58 [PubMed: 25639943]

30. Severcan F, Gorgulu G, Gorgulu ST, Guray T (2005) Rapid monitoring of diabetes-induced lipid peroxidation by Fourier transform infrared spectroscopy: evidence from rat liver microsomal membranes. Anal Biochem 339:36–40 [PubMed: 15766707]

31. Iwasaki Y, Kazama JJ, Yamato H, Fukagawa M (2011) Changes in chemical composition of cortical bone associated with bone fragility in rat model with chronic kidney disease. Bone 48:1260–1267 [PubMed: 21397740]

32. Tarnowski CP, Ignelzi MA Jr, Morris MD (2002) Mineralization of developing mouse calvaria as revealed by Raman microspectroscopy. J Bone Miner Res 17:1118–1126 [PubMed: 12054168]

33. Unal M, Yang S, Akkus O (2014) Molecular spectroscopic identification of the water compartments in bone. Bone 67:228–236 [PubMed: 25065717]

34. McNerny EMB, Gong B, Morris MD, Kohn DH (2015) Bone Fracture Toughness and Strength Correlate With Collagen Cross-Link Maturity in a Dose-Controlled Lathyrism Mouse Model. Journal of Bone and Mineral Research 30:455–464 [PubMed: 25213475]

35. Pascart T, Cortet B, Olejnik C, et al. (2016) Bone Samples Extracted from Embalmed Subjects Are Not Appropriate for the Assessment of Bone Quality at the Molecular Level Using Raman Spectroscopy. Anal Chem 88:2777–2783 [PubMed: 26824493]

36. Lane NE, Yao W, Balooch M, et al. (2005) Glucocorticoid-Treated Mice Have Localized Changes in Trabecular Bone Material Properties and Osteocyte Lacunar Size That Are Not Observed in Placebo-Treated or Estrogen-Deficient Mice. Journal of Bone and Mineral Research 21:466–476 [PubMed: 16491295]

37. Kazanci M, Wagner HD, Manjubala NI, et al. (2007) Raman imaging of two orthogonal planes within cortical bone. Bone 41:456–461 [PubMed: 17602910]

38. Gamsjaeger S, Masic A, Roschger P, et al. (2010) Cortical bone composition and orientation as a function of animal and tissue age in mice by Raman spectroscopy. Bone 47:392–399 [PubMed: 20450992]

39. Perry DA, Salvin JW, Romfh P, et al. (2017) Responsive monitoring of mitochondrial redox states in heart muscle predicts impending cardiac arrest. Sci Transl Med 9.: 10.1126/scitranslmed.aan0117

40. Kallepitis C, Bergholt MS, Mazo MM, et al. (2017) Quantitative volumetric Raman imaging of three dimensional cell cultures. Nat Commun 8:14843 [PubMed: 28327660]

41. Jiang X, Malkovskiy AV, Tian W, et al. (2014) Promotion of airway anastomotic microvascular regeneration and alleviation of airway ischemia by deferoxamine nanoparticles. Biomaterials 35:803–813 [PubMed: 24161166]

42. Penner JC, Ferreira JAG, Secor PR, et al. (2016) Pf4 bacteriophage produced by Pseudomonas aeruginosa inhibits Aspergillus fumigatus metabolism via iron sequestration. Microbiology 162:1583–1594 [PubMed: 27473221]

43. Zambelli VO, Gross ER, Chen C-H, et al. (2014) Aldehyde dehydrogenase-2 regulates nociception in rodent models of acute inflammatory pain. Sci Transl Med 6:251ra118

44. Osei-Sarfo K, Tang X-H, Urvalek AM, et al. (2013) The molecular features of tongue epithelium treated with the carcinogen 4-nitroquinoline-1-oxide and alcohol as a model for HNSCC. Carcinogenesis 34:2673–2681 [PubMed: 23784083]

45. Urvalek AM, Osei-Sarfo K, Tang X-H, et al. (2015) Identification of Ethanol and 4-Nitroquinoline-1-Oxide Induced Epigenetic and Oxidative Stress Markers During Oral Cavity Carcinogenesis. Alcoholism: Clinical and Experimental Research 39:1360–1372

46. Kawamoto T (2003) Use of a new adhesive film for the preparation of multi-purpose fresh-frozen sections from hard tissues, whole-animals, insects and plants. Arch Histol Cytol 66:123–143 [PubMed: 12846553]

47. Bergmann B, Mölne J, Gjertsson I (2015) The Bone-Inflammation-Cartilage (BIC) Stain: A Novel Staining Method Combining Safranin O and Van Gieson's Stains. J Histochem Cytochem 63:737–740 [PubMed: 26021335]

48. Rumin J, Bonnefond H, Saint-Jean B, et al. (2015) The use of fluorescent Nile red and BODIPY for lipid measurement in microalgae. Biotechnol Biofuels 8:42 [PubMed: 25788982]

49. Howell NK, Herman H, Li-Chan ECY (2001) Elucidation of Protein–Lipid Interactions in a Lysozyme–Corn Oil System by Fourier Transform Raman Spectroscopy. Journal of Agricultural and Food Chemistry 49:1529–1533 [PubMed: 11312891]

50. Sadeghi-Jorabchi H, Hendra PJ, Wilson RH, Belton PS (1990) Determination of the total unsaturation in oils and margarines by Fourier transform Raman spectroscopy. J Am Oil Chem Soc 67:483–486

51. Krempien B, Manegold C, Ritz E, Bommer J (1976) The influence of immobilization on osteocyte morphology. Virchows Arch 370:55–68

52. Schie IW, Nolte L, Pedersen TL, et al. (2013) Direct comparison of fatty acid ratios in single cellular lipid droplets as determined by comparative Raman spectroscopy and gas chromatography. Analyst 138:6662–6670 [PubMed: 24000336]

53. Meksiarun P, Andriana BB, Matsuyoshi H, Sato H (2016) Non-invasive Quantitative Analysis of Specific Fat Accumulation in Subcutaneous Adipose Tissues using Raman Spectroscopy. Sci Rep 6:37068 [PubMed: 27845402]

54. Bonifacio A, Sergo V (2010) Effects of sample orientation in Raman microspectroscopy of collagen fibers and their impact on the interpretation of the amide III band. Vib Spectrosc 53:314–317

55. Grosse RL (2002) Handbook of Raman Spectroscopy: From the Research Laboratory to the Process Line Edited by Ian R. Lewis (Kaiser Optical Systems) and Howell G. M. Edwards (University of Bradford). Dekker: New York, Basel. 2001. xiv + 1054 pp. $225. ISBN 0-8247-0557-2. J Am Chem Soc 124:5601–5602

56. Turner RT, Greene VS, Bell NH (2009) Demonstration that ethanol inhibits bone matrix synthesis and mineralization in the rat. Journal of Bone and Mineral Research 2:61–66

57. Maddalozzo GF, Turner RT, Edwards CHT, et al. (2009) Alcohol alters whole body composition, inhibits bone formation, and increases bone marrow adiposity in rats. Osteoporos Int 20:1529–1538 [PubMed: 19238309]

58. Akkus O, Adar F, Schaffler MB (2004) Age-related changes in physicochemical properties of mineral crystals are related to impaired mechanical function of cortical bone. Bone 34:443–453 [PubMed: 15003792]

59. Buckley K, Matousek P, Parker AW, Goodship AE (2012) Raman spectroscopy reveals differences in collagen secondary structure which relate to the levels of mineralisation in bones that have evolved for different functions. J Raman Spectrosc 43:1237–1243

60. Maurel DB, Benaitreau D, Jaffré C, et al. (2014) Effect of the alcohol consumption on osteocyte cell processes: a molecular imaging study. J Cell Mol Med 18:1680–1693 [PubMed: 23947793]

61. You L-D, Weinbaum S, Cowin SC, Schaffler MB (2004) Ultrastructure of the osteocyte process and its pericellular matrix. Anat Rec A Discov Mol Cell Evol Biol 278:505–513 [PubMed: 15164337]

62. Coleman RA, Young BM, Turner LE, Cook RT (2008) A practical method of chronic ethanol administration in mice. Methods Mol Biol 447:49–59 [PubMed: 18369910]

63. D'Souza El-Guindy NB, Kovacs EJ, De Witte P et al. (2010) Laboratory Models Available to Study Alcohol-Induced Organ Damage and Immune Variations: Choosing the Appropriate Model. Alcoholism: Clinical and Experimental Research 34:1489–1511

64. Ghanim H, Aljada A, Hofmeyer D, et al. (2004) Circulating mononuclear cells in the obese are in a proinflammatory state. Circulation 110:1564–1571 [PubMed: 15364812]
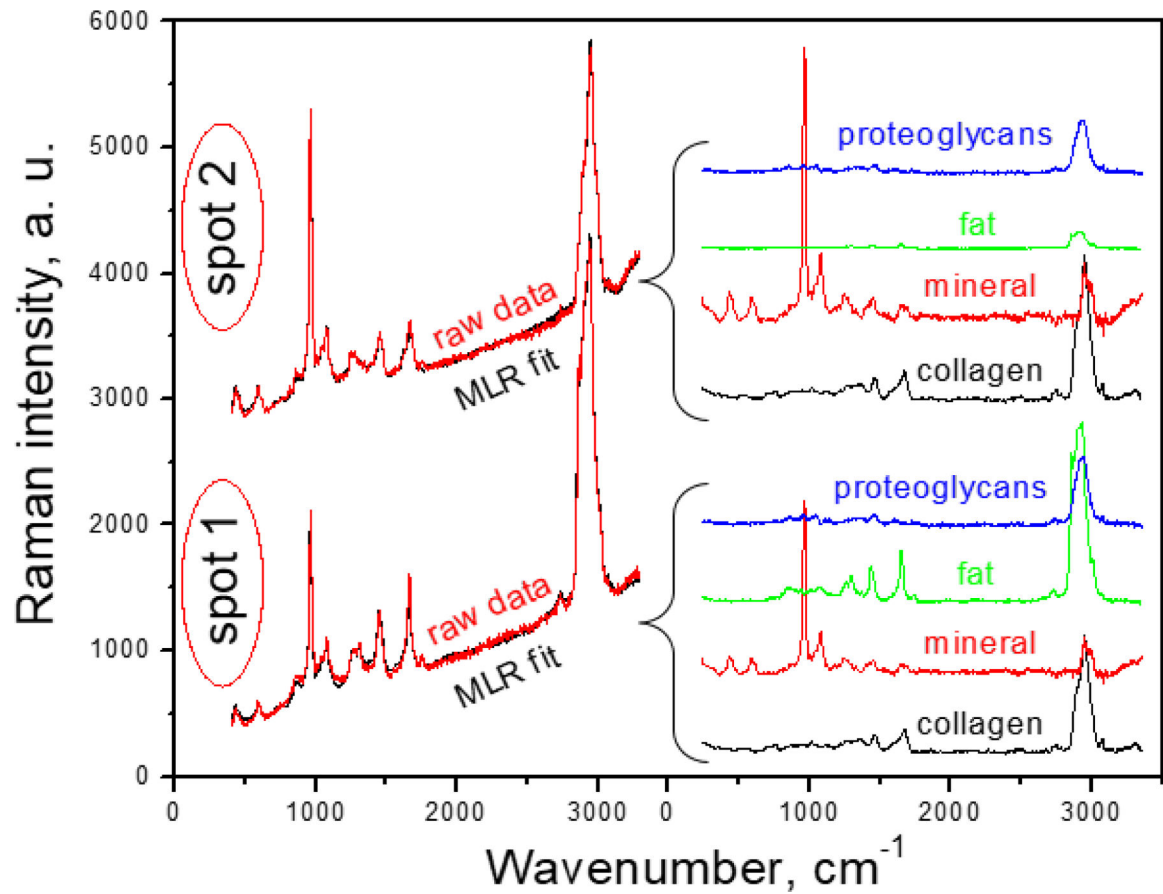
Fig. 1.
Example of Raman spectra from two spots within a bone section (left panel): raw data (black curve) and MLR fit (red curve) as a sum of purified spectra for the major sub-components of Raman spectra (right panel). Spot #1 is from an osteocyte location, spot #2 is typical of cell-free mineral/collagen matrix
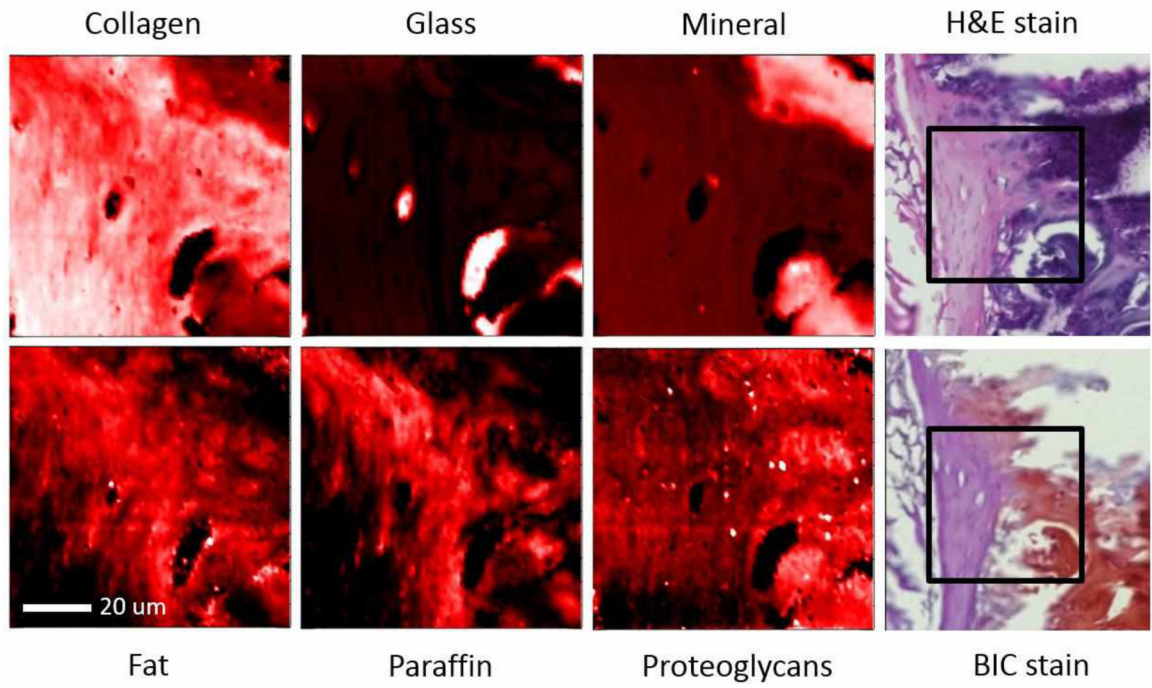
Fig. 2.
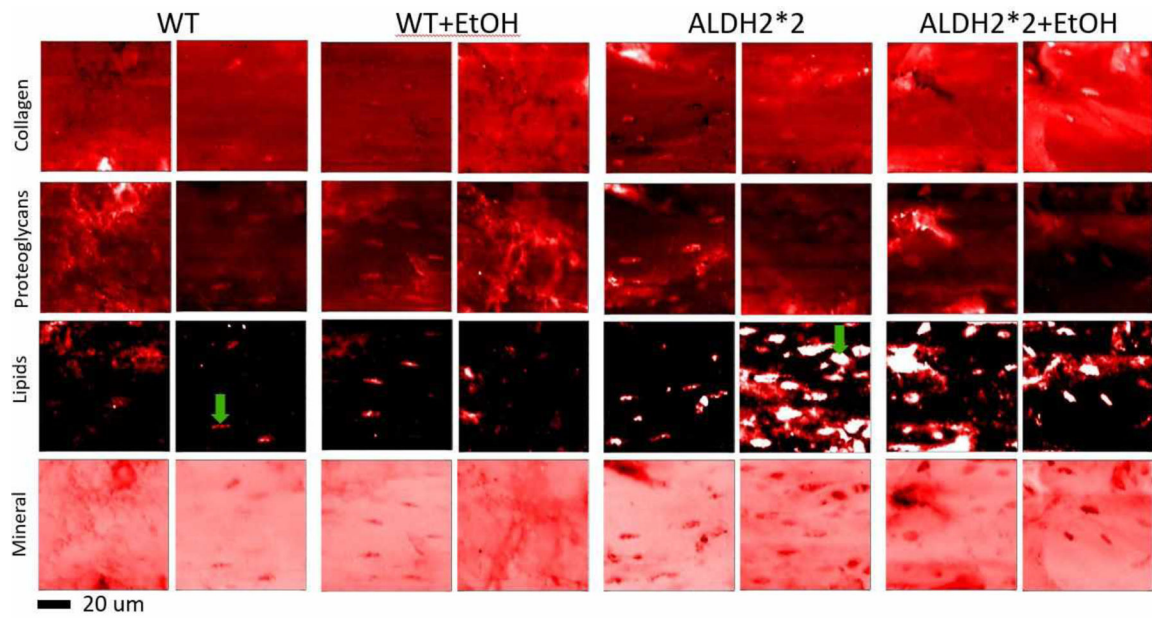MLR fit maps for sections made from bones embedded in paraffin

Fig. 3.
Selected MLR fit maps (two for each condition) of bone, mineral, bound proteoglycan and fat components for four different types of mouse femur samples: WT, WT and ethanol treatment, ALDH2*2/*2, ALDH2*2/*2 with ethanol treatment, as indicated. All vertical contrast scales are matched in each row. Green arrow marks typical osteocytes in WT and ALDH2*2/*2 samples, the latter also corresponds to the spot for the Raman spectrum of fat in Fig. S1a
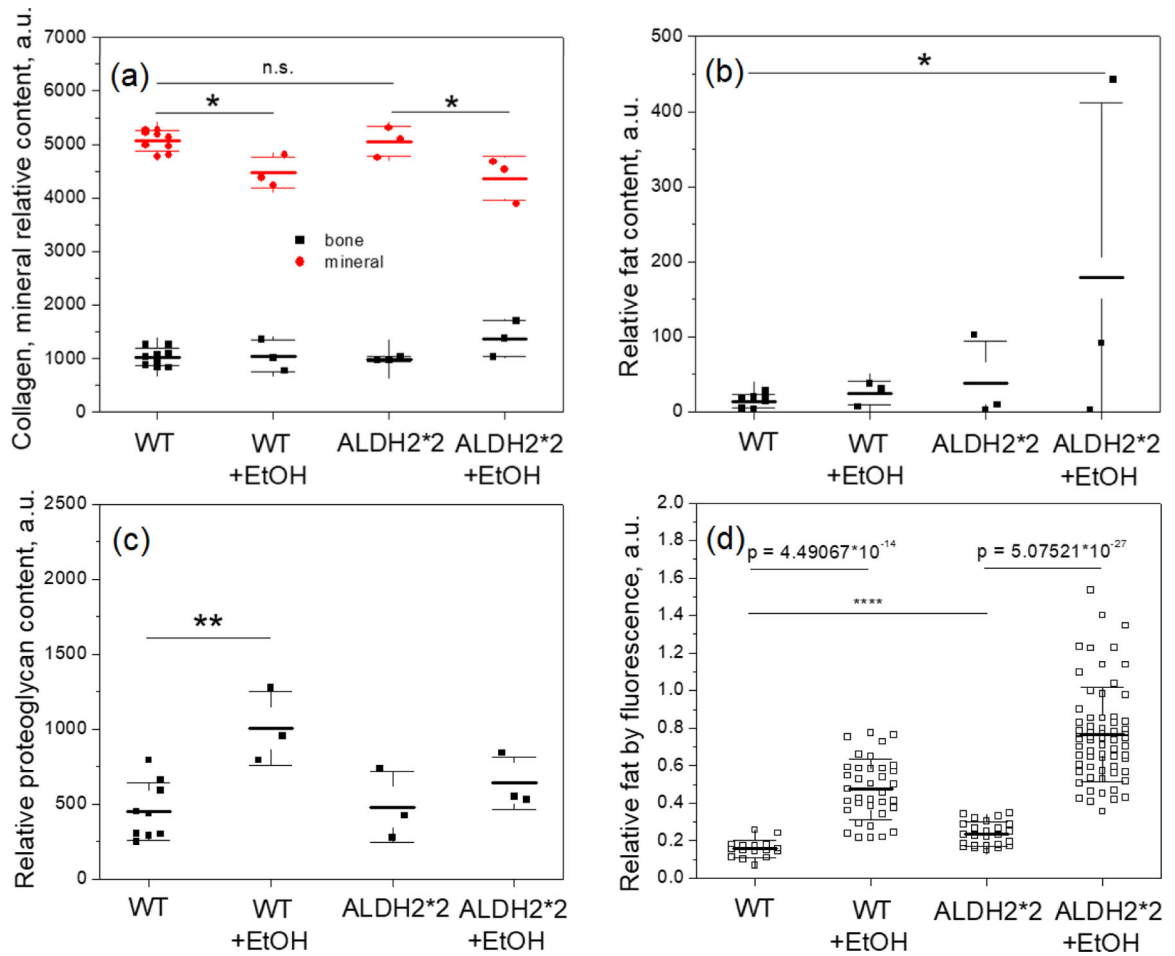
Fig. 4.
Raman and fluorescence imaging was performed for regions in the middle of the cortical bone. Relative collagen, mineral, fat and bound proteoglycan content for four types of mouse femur samples: (a) collagen, mineral relative content for the individual groups, (b) fat relative content for the individual groups, (c) bound proteoglycan content for the individual groups. (d) Average normalized magnitude of fat signal inside osteocytes. Every data-point represents one osteocyte. Error bars are mean values ± SD. Number of individual animals is 9 for WT and 3 per other groups. Statistical significance was measured using non-parametric permutation tests (a-c) and t-tests with Welch's adjustment for differing variances (d). Significance levels are marked as follows: * $p < 0.05$ (mineral WT to WT+EtOH), **$p < 0.05$ (proteoglycan WT to WT+EtOH)
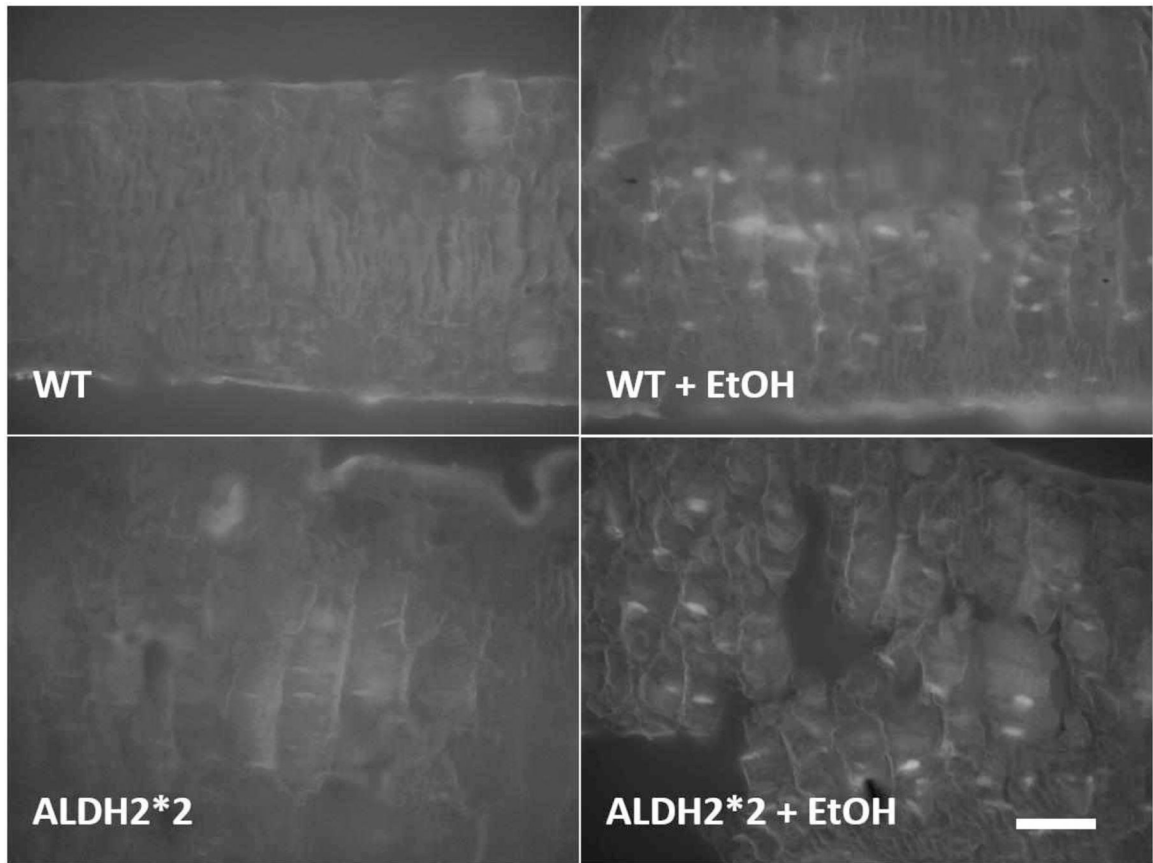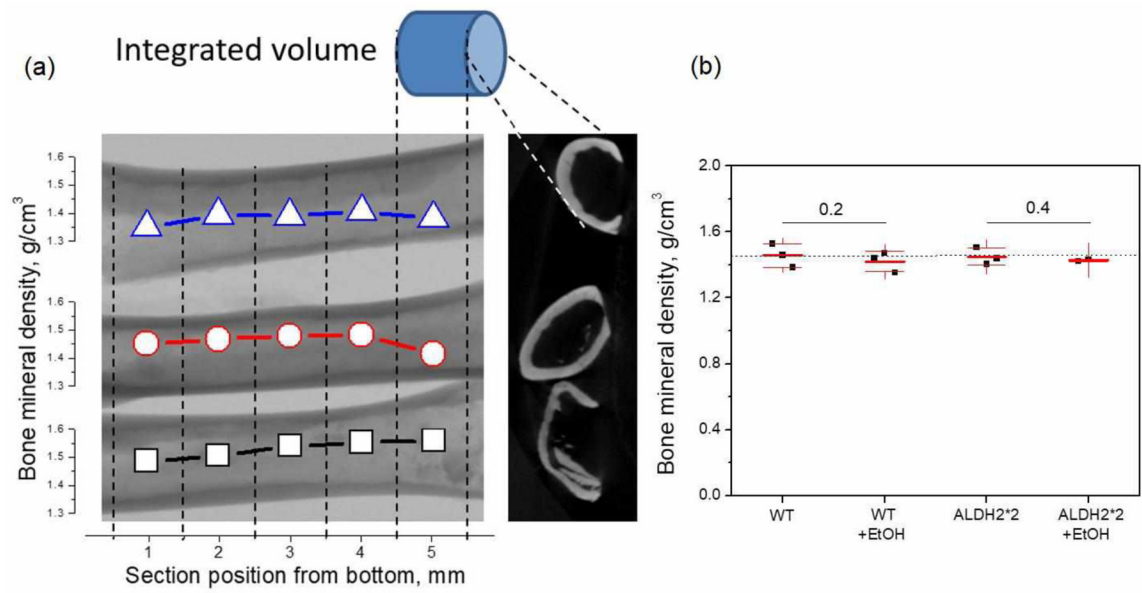
Fig. 5.
Maps of Nile Red fluorescent stain for WT, WT+EtOH, ALDH2*2 and ALDH2*2+EtOH sections, showing elevated fat content in osteocytes for mice consuming alcohol and those with ALDH2*2 mutation. Scale bar is 50 μm. The quantified data is shown in Fig. 4d.

Fig. 6.
(a) Bone mineral densities of 1 mm-long subsections along three WT bones, overlaid on top of front maximum intensity projection, top-view single X-Ray section is shown to the right of the graph (b) Bone mineral density for four sample types with symbols for every 1 mm section, showing the same trend as Raman data, but lack of statistical significance between groups, as measured by Wilcoxon independent test. Dashed line added as guide for the eye